



Research Paper

Boosting visible light photoreactivity of photoactive metal-organic framework: Designed plasmonic Z-scheme Ag/AgCl@MIL-53-Fe



Qiuxia Liu, Chunmei Zeng, Lunhong Ai*, Zhen Hao, Jing Jiang*

Chemical Synthesis and Pollution Control Key Laboratory of Sichuan Province, College of Chemistry and Chemical Engineering, China West Normal University, Nanchong 637002, PR China

ARTICLE INFO

Keywords:

Photoreactivity
Metal-organic framework
Ag/AgCl
Dye degradation
Cr(VI) reduction

ABSTRACT

In this work, we report the efficient integration of plasmonic Ag/AgCl with a typical photoactive metal-organic framework (MOF, MIL-53-Fe) to boost the visible light photoreactivity of MOFs. The Ag/AgCl@MIL-53-Fe photocatalysts are rationally designed and successfully prepared by a facile one-pot solvothermal route, where the Ag/AgCl nanoparticles are firmly anchored on the surface of MIL-53-Fe microrods. The formed structure is in favor of the synergistic transfer of photoinduced electrons and holes in the Ag/AgCl@MIL-53-Fe by a Z-scheme mechanism, ensuring the long lifetime of charge carriers and yielding the enhanced photocatalytic activity. The photocatalytic experiments reveal that Ag/AgCl@MIL-53-Fe is highly efficient for organic pollutant degradation and Cr(VI) reduction under visible light irradiation. The photocatalytic reactivity of Ag/AgCl@MIL-53-Fe is about 21.4 times and 10.8 times higher than that of bare MIL-53-Fe for the degradation of RhB and reduction of aqueous Cr(VI), respectively. Our finding on photoredox of Ag/AgCl@MIL-53-Fe would bring new insight into the design and development of highly efficient MOF-based photocatalysts.

1. Introduction

Metal-organic frameworks (MOFs) are newly emerged as a class of crystalline and microporous materials, which are constructed from metal cations/clusters interconnected with organic linkers [1]. Their outstanding features including large surface area, well-defined porosity, and tailororable functionality endow them with great promise in gas storage [2], separation [3], and catalysis [4]. Especially, the photoactive MOFs intrinsically interact with incident light and exhibit semiconducting performance, and they can photocatalytically driven various chemically useful photoredox reactions, bearing on ligand-to-metal charge transfer (LMCT) and/or direct metal-oxo cluster excitation [5,6]. In this context, a series of photoactive MOFs have exploited as potential candidates for photocatalysis, including ZIFs and MILs [7–10]. Among them, MIL-53-Fe has been considered as a typical iron-based MOF with photoreactivity due to its flexible structure, nontoxicity, and intrinsically optical absorbance. The MIL-53-Fe has a suitable optical band gap of about 2.6 eV, which has ability towards organic dye degradation. Our earlier observations have observed that the visible light photoreactivity of bare MIL-53-Fe is still moderate and not satisfactory, which is needed the assistant of hydrogen peroxide to increase concentration of active species [11]. To further enhance visible light activity, the combination of other functional materials with MIL-53-Fe is

also required [12,13].

The surface plasmon resonance (SPR) of noble metal nanoparticles has recently been introduced into visible light photocatalysis owing to the significantly amplified absorption in the visible light region [14,15]. In particular, the silver/silver halides (Ag/AgX, X = Cl, Br) are a characteristic composite-type plasmonic photocatalysts, which are capable of generating highly active charge carriers under visible light irradiation to achieve rapid degradation of various organic pollutants [16,17]. In addition, Ag/AgX has been reported as an efficient second photocatalytic component to modify the conventional semiconductor photocatalysts [18,19], such as TiO₂ [20], BiOX [21], BiVO₄ [22], Bi₂WO₆ [23], and C₃N₄ [24], realizing the greatly enhanced visible light photoreactivity. They can not only introduce a new source for light absorption due to the SPR effect of Ag nanoparticles but also improve the separation efficiency of charge carriers because of the energy-matched band structure. Despite these exciting advances, we note that the current research mainly focuses on Ag/AgX-modified inorganic semiconductor photocatalytic systems. Some questions naturally arise at this point: (i) do the Ag/AgX as a booster to realize the enhanced visible light photocatalytic activity of MOFs? (ii) Whether the role of Ag/AgCl in MOF-based photocatalytic systems is similar to previously reported inorganic semiconductor systems? Furthermore, the MOFs possess the distinguished structure feature to offer the large

* Corresponding authors.

E-mail addresses: ah_ahong@163.com (L. Ai), 0826zjh@163.com (J. Jiang).

accommodation space for reactant diffusion and adsorption due to their accessible pores and open channels. Therefore, it is of great interest to systematically study the photocatalysis process of Ag/AgX@MOFs.

Our previous observation has been suggested that MIL-53-Fe is a good host matrix to load inorganic nanomaterials for implementation of the desired properties [13], which facilitates the homogeneous dispersion of the inorganic nanoparticles on their surface and avoid the nanoparticles aggregation. In this study, we further demonstrate the efficient integration of a plasmonic Ag/AgCl with a photoactive MIL-53-Fe greatly boosts the visible light photoreactivity of MOFs by a Z-scheme mechanism. Such structure is in favor of the synergistic transfer of photoinduced electrons and holes in the Ag/AgCl@MIL-53-Fe. The resulting Ag/AgCl@MIL-53-Fe is highly efficient for photooxidation of organic dyes and photoreduction of aqueous Cr(VI) under visible light irradiation, and its photocatalytic reactivity is about 21.4 times and 10.8 times higher than that of bare MIL-53-Fe for the photooxidation and photoreduction reactions, respectively. Our finding on photoredox of Ag/AgCl@MIL-53-Fe would bring new insight into the design and development of highly efficient MOF-based photocatalysts.

2. Experimental

2.1. Materials

$\text{FeCl}_3 \cdot 6\text{H}_2\text{O}$, 1,4-benzenedicarboxylic acid (1,4-BDC), AgNO_3 , N,N -dimethylformamide (DMF), Rhodamine B (RhB), methylene blue (MB), *p*-nitrophenol, potassium dichromate, CCl_4 , disodiummethylenediamine tetraacetate (EDTA), *tert*-butylalcohol (TBA), 1,5-diphenylcarbazide (DPC), H_3PO_4 and acetone were purchased from Kelong Chemical Reagents Company (Chengdu, China). All chemicals used in this study were of analytical grade and used without further purification.

2.2. Synthesis of Ag/AgCl@MIL-53-Fe (AAM) photocatalysts

In a typical procedure, 1 mmol of 1,4-BDC, 0.67 mmol of $\text{FeCl}_3 \cdot 6\text{H}_2\text{O}$ and 0.33 mmol of AgNO_3 were added slowly into 5 mL of DMF solution. The mixture was stirred for 10 min at room temperature, and then transferred to a 20 mL Teflon-lined autoclave that was sealed and heated at 150 °C for 12 h. After the reaction, the autoclave was allowed to cool naturally to room temperature. The resulting precipitates were collected by centrifugation at 6000 rpm for 2 min. To remove the solvent, the obtained solids were suspended into a 200 mL of distilled water overnight and then centrifuged and dried in vacuum at 60 °C for 12 h. By changing the Fe:Ag ratio but keeping total metal:ligand ratios of 1:1, the different Ag/AgCl@MIL-53-Fe samples can be prepared under the same conditions. The corresponding sample was designated as AAM-0 (Fe:Ag = 1:0), AAM-1 (Fe:Ag = 5:1), AAM-2 (Fe:Ag = 2:1), and AAM-3 (Fe:Ag = 1:1). For comparison, the Ag/AgCl was also synthesized under the same condition by replacing 1,4-BDC and $\text{FeCl}_3 \cdot 6\text{H}_2\text{O}$ with the required amount of NaCl.

2.3. Characterization

The powder X-ray diffraction (XRD) measurements were recorded on a Rigaku Dmax/Ultima IV diffractometer with monochromatized Cu K α radiation ($\lambda = 0.15418$ nm). The morphology was observed with a field emission scanning electron microscope (FESEM, Hitachi S4800) and a transmission electron microscope (TEM, FEI Tecnai G20). The elemental composition of the samples were characterized by energy-dispersing X-ray spectroscopy (EDS, Oxford instruments X-Max). X-ray photoelectron spectroscopy (XPS) measurements were recorded on a Perkin-Elmer PHI 5000C spectrometer using monochromatized Al K α excitation. All binding energies were calibrated by using the contaminant carbon ($C_{1s} = 284.6$ eV) as a reference. The Fourier transform infrared (FTIR) spectroscopy was recorded on Nicolet 6700 FTIR Spectrometric Analyzer using KBr pellets. UV-vis diffuse reflectance

spectra of the samples were obtained for the dry-pressed film samples using a UV-vis spectrophotometer (UV-3600, Shimadzu, Japan). BaSO_4 was used as a reflectance standard in a UV-vis diffuse reflectance experiment. Photoluminescence (PL) spectroscopy was performed on a Cary Eclipse fluorescence spectrometer excited by incident light of 350 nm.

2.4. Electrochemical measurements

For the preparation of working electrode, 5 mg of as-prepared catalyst powders were mixed with 1 mL of ethanol and 10 μL of nafion homogeneously. The 100 μL of dispersion was then drop-casted onto an indium-tin oxide (ITO) glass electrode with coated area of 1 cm^2 for the electrochemical measurements. The transient photocurrent, electrochemical impedance spectra (EIS) and Mott-Schottky tests were performed on an electrochemical workstation (CHI 660E, CH Instruments Inc., Shanghai) in a typical three-electrode setup with an electrolyte solution of 0.5 M Na_2SO_4 , using a Pt foil as the counter electrode, a saturated calomel electrode (SCE) as the reference electrode and modified ITO glass as the working electrode.

2.5. Evaluation of photoreactivity

The photooxidation ability of Ag/AgCl@MIL-53-Fe were tested by degradation of RhB aqueous solution under visible light irradiation, which were conducted in a cylindrical Pyrex vessel reactor using a 500 W Xe arc lamp with a 420 nm cutoff filter as the light source. Typically, 0.01 g of photocatalyst sample was added into 25 mL of 10 mg L⁻¹ RhB aqueous solution. The suspension was magnetically stirred in the dark for 30 min to establish the adsorption desorption equilibrium. After visible light illumination, 2 mL samples were taken out at predetermined time intervals and separated by centrifugation. The concentration of RhB left in the supernatant solution was determined by using a Shimadzu UV2550 UV-vis spectrophotometer at its maximum absorption wavelength of 554 nm. The photoreduction ability of Ag/AgCl@MIL-53-Fe was also examined by photocatalytic reduction of 10 mg L⁻¹ hexavalent Cr(VI) under visible light under identical conditions. The concentrations of Cr(VI) were determined by a Shimadzu UV-2550 UV-vis spectrophotometer using the diphenylcarbazide (DPC) method, which is in terms of the reaction between Cr(VI) and DPC to form a red-purple chromium 1,5-diphenylcarbazide complex.

3. Results and discussion

Fig. 1 shows the typical X-ray diffraction (XRD) patterns of the as-synthesized Ag/AgCl and Ag/AgCl@MIL-53-Fe (AAM). The Ag/AgCl

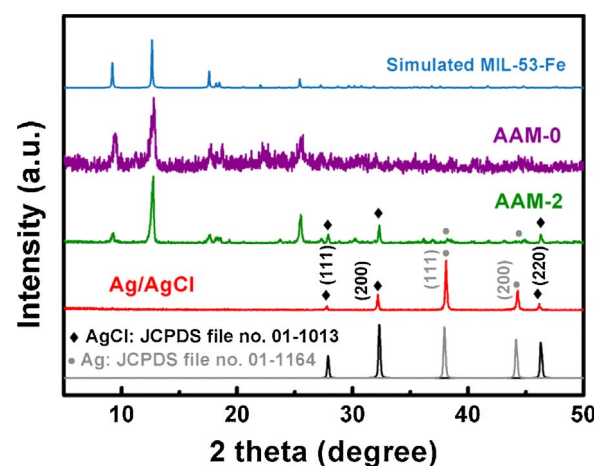


Fig. 1. XRD patterns of Ag/AgCl, MIL-53-Fe and Ag/AgCl@MIL-53-Fe samples.

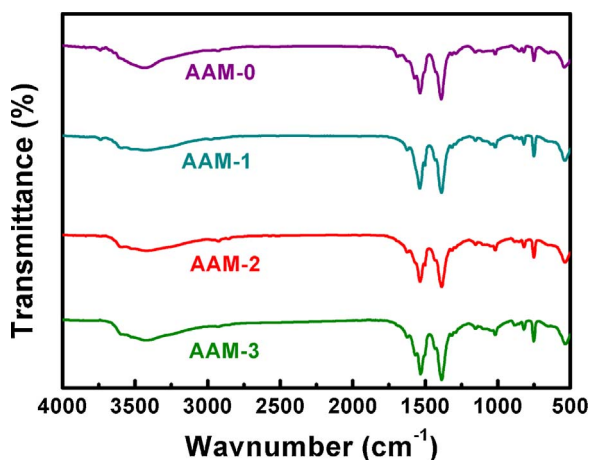


Fig. 2. FTIR spectra of different Ag/AgCl@MIL-53-Fe samples.

prepared in DMF is composed of a cubic AgCl phase (JCPDS file no. 01-1013) and a metallic Ag phase (JCPDS file no. 01-1164). The bare MIL-53-Fe displays the characteristic peaks at 9.4, 12.7, 17.6 and 25.4°, which is in good agreement with the simulated and previously reported XRD patterns of crystalline MIL-53 MOFs [13,25]. Similarly, the phase structure of the MIL-53-Fe mainly exists in the Ag/AgCl@MIL-53-Fe products as well. Meanwhile, other characteristic diffraction peaks can be also observed at 27.8, 32.3, and 46.3° corresponding to the (111), (200), and (220) reflections of cubic phase AgCl, respectively. Moreover, an additional weak peak at 38.2° is also visible in all the XRD patterns of Ag/AgCl@MIL-53-Fe, matching with the (111) plane of the metallic Ag with cubic phase. Notably, there is no shift in the peak positions of MIL-53-Fe in the pattern of the Ag/AgCl@MIL-53-Fe, suggesting that the integration of Ag/AgCl with MIL-53-Fe did not destroy the crystal structure of the framework.

The molecular structure of the Ag/AgCl@MIL-53-Fe was further investigated by FTIR spectroscopy. The general features of FTIR spectra (Fig. 2) for these Ag/AgCl@MIL-53-Fe samples are almost identical to those of reported MIL-53-Fe [12,13]. The characteristic absorption bands at 1536 and 1392 cm⁻¹ are ascribed to asymmetric ($\nu_{as}(C-O)$) and symmetric ($\nu_s(C-O)$) vibrations of the carboxyl groups, respectively, revealing the existence of dicarboxylate linker within the framework. The bands at 1629 cm⁻¹ (C=C stretching vibration) and 756 cm⁻¹ (C–H bending vibrations) are characteristic of benzene rings. Meanwhile, a band at 542 cm⁻¹ in the low-frequency region also evidences the typical Fe–O stretching vibrations in framework.

The morphology and microstructure of the as-prepared Ag/AgCl@MIL-53-Fe products were examined by scanning electron microscopy (SEM) and transmission electron microscopy (TEM). Fig. 3a shows a typical low magnification SEM image of the bare MIL-53-Fe. It is clear that the MIL-53-Fe is composed of a large number of microrods with diameters of 2–5 μm and lengths of several tens of micrometers. The high-magnification image (Fig. 3b) further reveals that the MIL-53-Fe microrods have straight edge, smooth and flat surface. Interestingly, the Ag/AgCl@MIL-53-Fe (AAM-2) products exhibit a similar shape to that of MIL-53-Fe (Fig. 3c), however, introduction of Ag species would induce the increase in dimension of MIL-53-Fe microrods. The diameters and lengths of MIL-53-Fe in resulting Ag/AgCl@MIL-53-Fe samples enlarged greatly. Meanwhile, the smooth surface became coarse (Fig. 3d) due to the surface coverage of Ag/AgCl nanoparticles. The corresponding elemental mapping images shown in Fig. 3e confirm the coexistence of C, O, Fe, Ag, and Cl elements in Ag/AgCl@MIL-53-Fe sample and reveal uniform distribution of these elements through the microrods. In addition, the quantitatively calculated surface mole ratio of Fe to Ag in Ag/AgCl@MIL-53-Fe from EDS spectrum (Fig. S1, Supporting Information) is approximately 2.25:1, which is slightly higher than its feeding ratio (2:1).

The detailed microstructures of the Ag/AgCl@MIL-53-Fe microrods were further determined by transmission electron microscopy (TEM). Fig. 4a is a representative TEM image of the Ag/AgCl@MIL-53-Fe (AAM-2) sample, which confirms the typical rod-like geometry of the products, consistent with that of SEM observations. It is clear that the Ag/AgCl nanoparticles are uniformly, densely and firmly anchored on the surfaces of the MIL-53-Fe microrods (Fig. 4b). HRTEM image of Ag/AgCl@MIL-53-Fe shown in Fig. 4c reveals clearly visible lattice fringes with spacing of 0.28 nm and 0.24 nm (see the line profile in Fig. 4d and e), corresponding to the cubic phase AgCl (111) plane and cubic phase metallic Ag (111) plane, respectively, confirming the effective loading of Ag/AgCl on the surface of MIL-53-Fe microrods.

The chemical state and surface composition of Ag/AgCl@MIL-53-Fe were further probed by X-ray photoelectron spectroscopy (XPS). Fig. 5a shows a typical survey scan of Ag/AgCl@MIL-53-Fe sample, which indicates that the Ag, Cl, Fe, C and O elements coexist in the resulting Ag/AgCl@MIL-53-Fe, agreeing well with above EDS analysis. The high resolution XPS spectrum of C 1s (Fig. 5b) is split into two distinct peaks, attributed to carbon species on benzene ring (283.9 eV) and carboxylate functional groups (287.8 eV). The high-resolution XPS spectrum of O 1s is displayed in Fig. 5c, which can be deconvoluted into Fe–O (529.6 eV) and oxygen species of carboxylate groups on BDC linkers (531.2 eV). Fig. 5d shows the high-resolution XPS spectrum of Fe 2p. The two well-defined peaks at binding energy of 711.1 and 725.0 eV with a satellite signal at 718.2 eV are characteristic of Fe³⁺ in MIL-53-Fe. Fig. 5e shows the high-resolution XPS spectrum of Ag 3d. The peaks with binding energies at around 366.6 and 372.5 are ascribed to Ag 3d_{5/2} and Ag 3d_{3/2} of Ag⁺ in AgCl, the those at binding energies of 374.5 and 368.2 eV, corresponding to the metallic Ag. In addition, the high-resolution XPS spectrum (Fig. 5f) of Cl 2p displays double peaks located at 197.5 and 199 eV, which can be assigned to the characteristic doublets of Cl 2p_{3/2} and Cl 2p_{1/2}, respectively.

The photoreactivity of the as-prepared Ag/AgCl@MIL-53-Fe was evaluated by the degradation of RhB under visible light. Before illumination, the adsorption performance of the Ag/AgCl@MIL-53-Fe for the RhB in the dark was first studied, as shown in Fig. S2. All the Ag/AgCl@MIL-53-Fe samples show a slight adsorption performance towards RhB. Obviously, the adsorption ability of Ag/AgCl@MIL-53-Fe on RhB molecules does not significantly affect their photocatalytic performances. The photodegradation curves of RhB solution over the Ag/AgCl@MIL-53-Fe are displayed in Fig. 6a. As observed, the RhB is relatively stable in the absence of photocatalysts under visible light irradiation. The bare MIL-53-Fe (AAM-0) is able to photodecompose RhB, but it only remove 20% of RhB under visible light irradiation for 45 min, reflecting the low efficiency of the MIL-53-Fe. By combination of Ag/AgCl, the resulting Ag/AgCl@MIL-53-Fe photocatalysts show the remarkably enhanced photocatalytic activity. Among all the samples, the AAM-2 exhibits the highest activity towards degradation of RhB, which can completely decompose 10 mg L⁻¹ of RhB under visible light illumination for 45 min. To gain insight into the photocatalytic kinetics, the reaction rates of the RhB photodegradation over AAM samples were calculated according to pseudo-first-order equation: $\ln(C/C_0) = kt$, where C is the concentration of the RhB at time t, C_0 is the initial concentration of the RhB solution, and the slope k is the reaction rate constant (min⁻¹), as shown in Fig. 6b. The reaction rate constants of the above photocatalysis processes were thus obtained by using corresponding plots ($\ln(C/C_0)-t$) and depicted in Fig. 6c. Thus, the rate constants of the AAM-0, AAM-1, AAM-2, and AAM-3 are calculated to be 0.005, 0.016, 0.107 and 0.049 min⁻¹, respectively. The quantitative analysis suggests that photocatalytic activity of Ag/AgCl@MIL-53-Fe (AAM-2) is about 21.4 times higher than that of MIL-53-Fe (AAM-0), indicating greatly enhanced photocatalytic performance of MIL-53-Fe by integrating Ag/AgCl. Furthermore, we also evaluated the stability of Ag/AgCl@MIL-53-Fe (AAM-2) by conducting the RhB degradation repeatedly five times. As shown in Fig. 6d, the AAM-2 can retain nearly unchanged catalytic activity after three cycles for the photodegradation

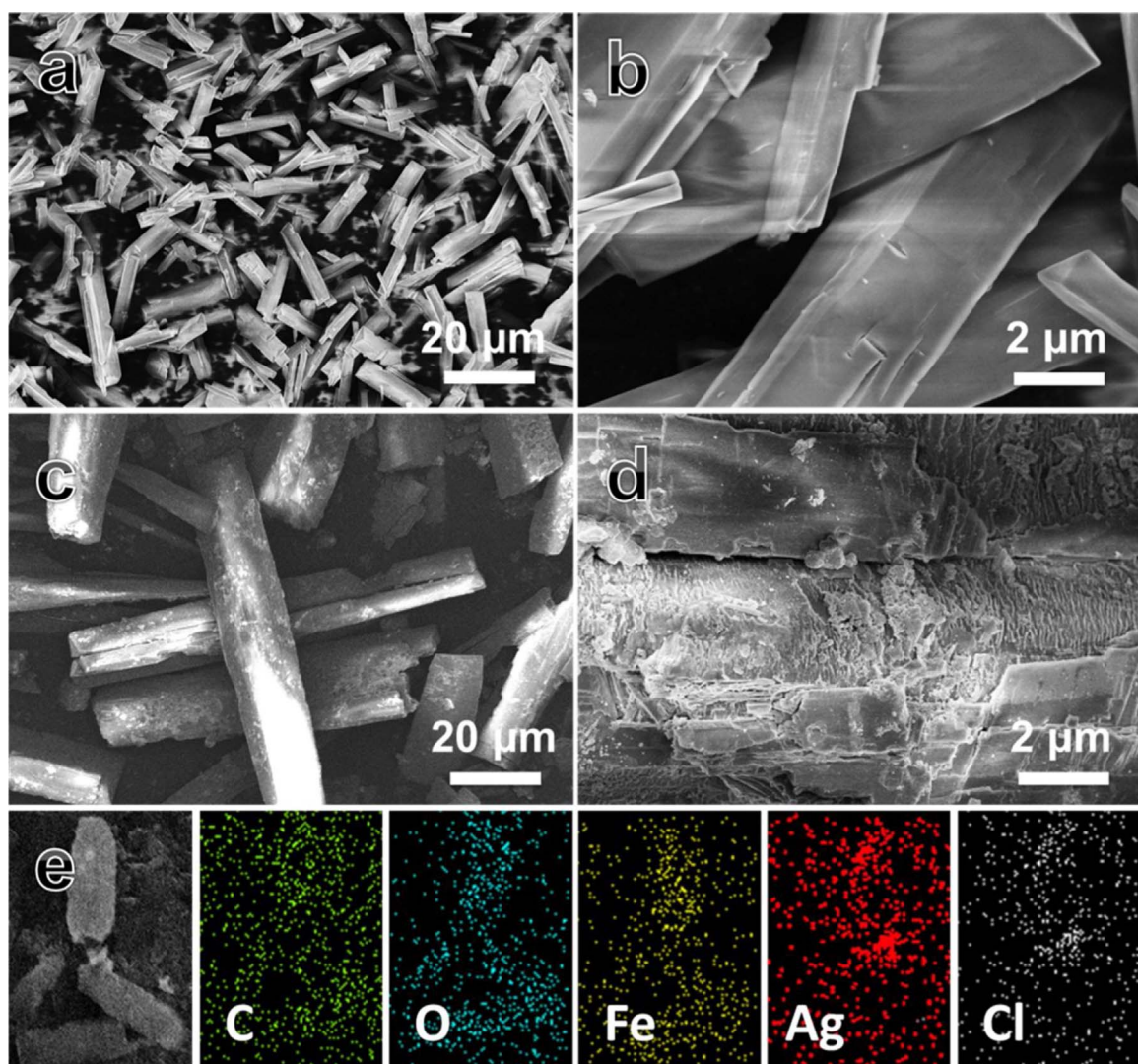


Fig. 3. SEM images of bare MIL-53-Fe (a,b) and Ag/AgCl@MIL-53-Fe (c,d). SEM-EDS mapping images of the Ag/AgCl@MIL-53-Fe.

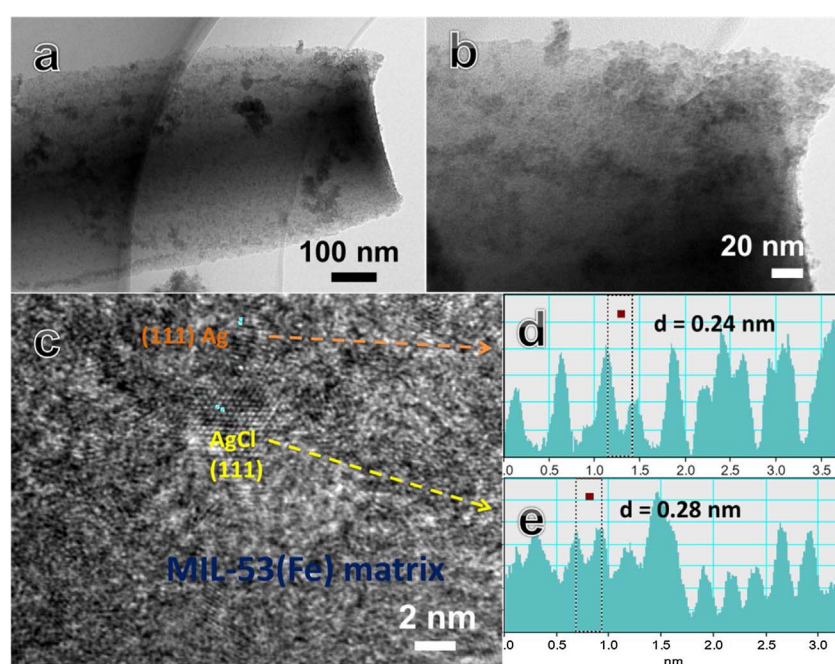


Fig. 4. TEM (a,b), HRTEM (c) images, and corresponding line profile (d,e) of Ag/AgCl@MIL-53-Fe.

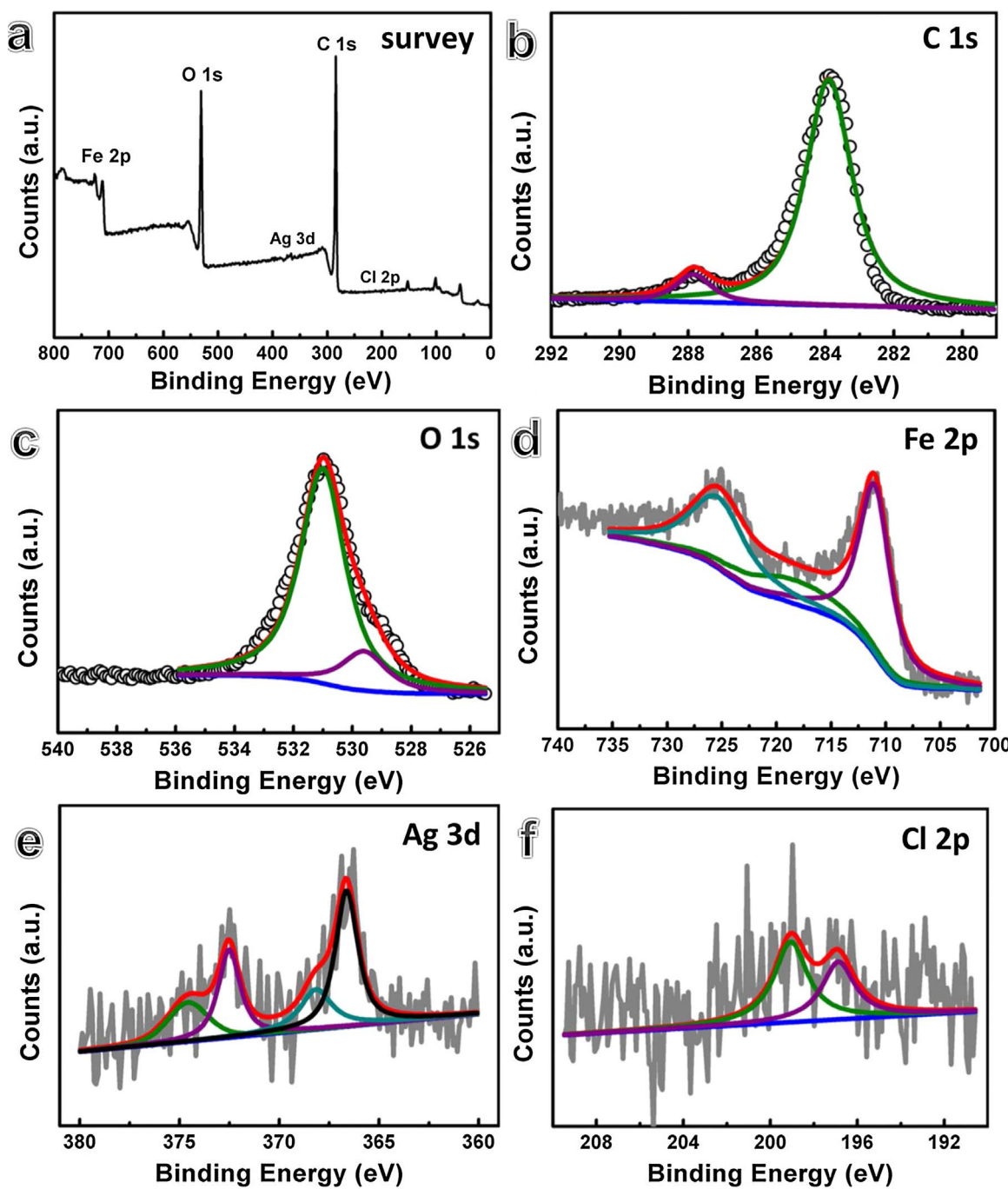


Fig. 5. XPS spectra of Ag/AgCl@MIL-53-Fe: (a) survey, (b) C 1s, (c) O 1s, (d) Fe 2p, (e) Ag 3d, and (f) Cl 2p.

of RhB. However, the declined activity is observed for further cycles, which could be caused by the catalyst mass loss during long-term photocatalytic tests. Moreover, the leaching of metal ions from photocatalysts after four photocatalytic cycles was determined by inductively coupled plasma optical emission spectroscopy (ICP-OES). It is found that the concentrations of dissolved iron ions and silver ion from the Ag/AgCl@MIL-53-Fe in reaction solution are extremely low after four photocatalytic cycles, consistent with previously reported Ag/AgCl-based photocatalysts [26,27]. Additionally, the XRD pattern and FTIR spectra of the Ag/AgCl@MIL-53-Fe before and after photocatalytic reaction present no obvious change in crystal phase and molecular structures for the photocatalysts (Fig. S3, Supporting Information). These results demonstrate that the Ag/AgCl@MIL-53-Fe is stable during photocatalytic process. Meanwhile, the photocatalytic activity of Ag/

AgCl@MIL-53-Fe was also tested by the degradation of MB under visible light. The data shown in Fig. 6e clearly demonstrates that Ag/AgCl@MIL-53-Fe (AAM-2) exhibits the highest photocatalytic activity for photodegrading MB among all the samples. Moreover, the photocatalytic degradation of *p*-nitrophenol (PNP) over the MIL-53-Fe and Ag/AgCl@MIL-53-Fe under visible light was also investigated. The Ag/AgCl@MIL-53-Fe still exhibits the better photocatalytic activity than that of bare MIL-53-Fe (Fig. S4, Supporting Information). These results confirm the enhanced photocatalytic performance of the Ag/AgCl@MIL-53-Fe.

In order to clarify the reactive species involved photocatalytic process for RhB degradation over Ag/AgCl@MIL-53-Fe, the active species trapping experiments were further conducted, where EDTA, CCl₄ and TBA were used as a scavenger for hole, electron and hydroxyl

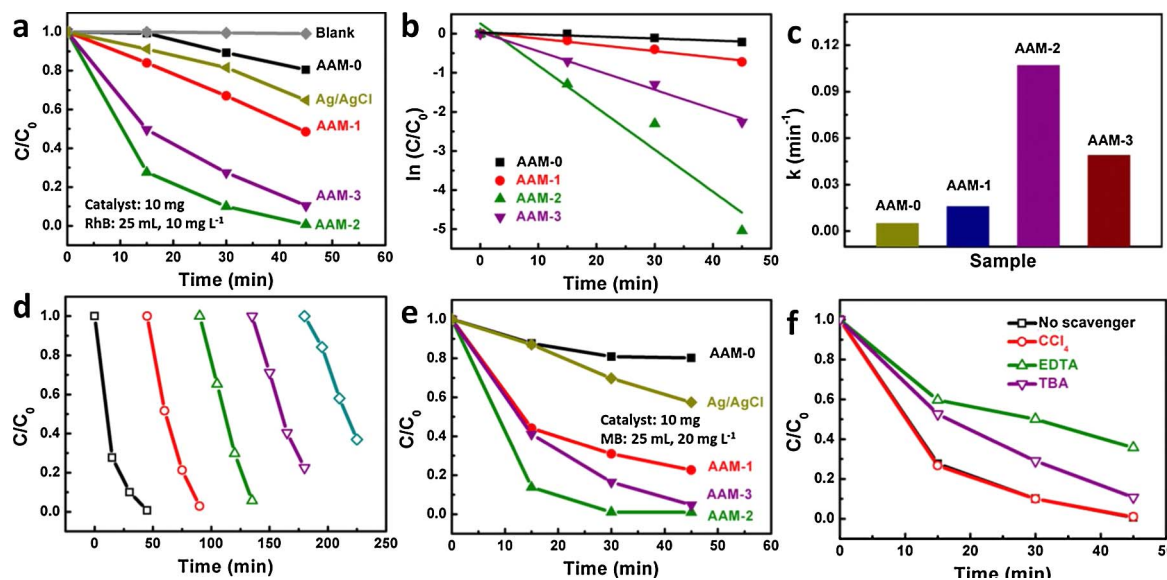


Fig. 6. (a) Photodegradation of RhB over different catalysts under visible light irradiation. (b) Photodegradation kinetics of RhB over different catalysts under visible light irradiation. (c) Comparison of the reaction rate constants of RhB photodegradation over different catalysts under visible light irradiation. (d) Recycling test on RhB photodegradation over Ag/AgCl@MIL-53-Fe (AAM-2) photocatalyst. (e) Photodegradation of MB over different catalysts under visible light irradiation. (f) Photodegradation of RhB over Ag/AgCl@MIL-53-Fe (AAM-2) photocatalyst in the presence of trapping systems.

radical ($\cdot\text{OH}$), respectively. Fig. 6f shows the photodegradation of RhB over Ag/AgCl@MIL-53-Fe in the presence different scavengers. The addition of EDTA and TBA can induce an obvious decrease in photocatalytic activity of Ag/AgCl@MIL-53-Fe, while the CCl₄ has no depression effect on the photodegradation of RhB. The quantitative analysis on photocatalytic depression efficiency further shows that EDTA, TBA and CCl₄ can yield about 35.3%, 10.2% and 0.3% inhibition on the photodegradation of RhB, respectively. This result confirms that photo-induced hole is the main radical species in the RhB photodegradation process.

Next, the photoreactivity of the as-prepared Ag/AgCl@MIL-53-Fe was also assessed by the photoreduction of Cr(VI) under visible light. Fig. 7a shows the photocatalytic reduction of aqueous Cr(VI) under visible light irradiation over the Ag/AgCl@MIL-53(Fe). Without catalyst, there is no change in Cr(VI) concentration under visible light irradiation, indicating that the direct photolysis is failed to drive the

reduction of Cr(VI). Instead, in the presence of catalysts, the photoreduction of aqueous Cr(VI) can be accelerated remarkably. As for bare MIL-53-Fe (AAM-0), it achieves 30% of reduction efficiency for Cr(VI) removal. This behavior can be further enhanced with the help of Ag/AgCl@MIL-53-Fe. Particularly, AAM-2 yields a highest reduction efficiency of 99.4% under visible light irradiation for 4 h. In terms of plots derived from pseudo-first-order equation (Fig. 7b), the photoreduction reaction rate constants in the presence of above catalysts can be obtained. As shown in Fig. 7c, the AAM-2 shows the highest reduction rate constant (1.002 h^{-1}), which is 10.8, 2.1, and 3.0 times as high as that of AAM-0 (0.093 h^{-1}), AAM-1 (0.485 h^{-1}), and AAM-3 (0.332 h^{-1}), respectively. To probe the stability of the Ag/AgCl@MIL-53-Fe (AAM-2) photocatalyst, the photoreduction of aqueous Cr(VI) was recycled for five times under same conditions. As shown in Fig. 7d, the Cr(VI) photoreduction efficiency of the AAM-2 catalyst is still up to 93% after five cycles, demonstrating its long-term stability for photoreduction of

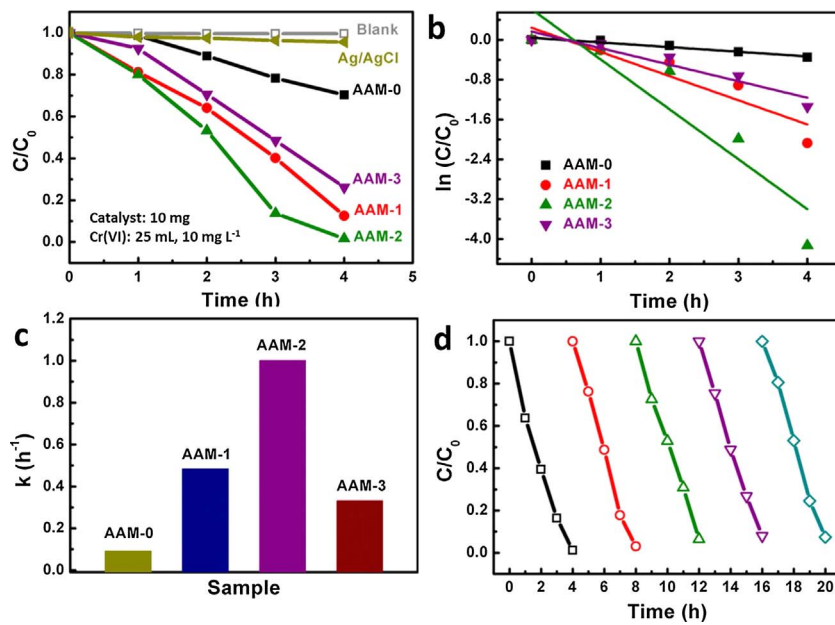
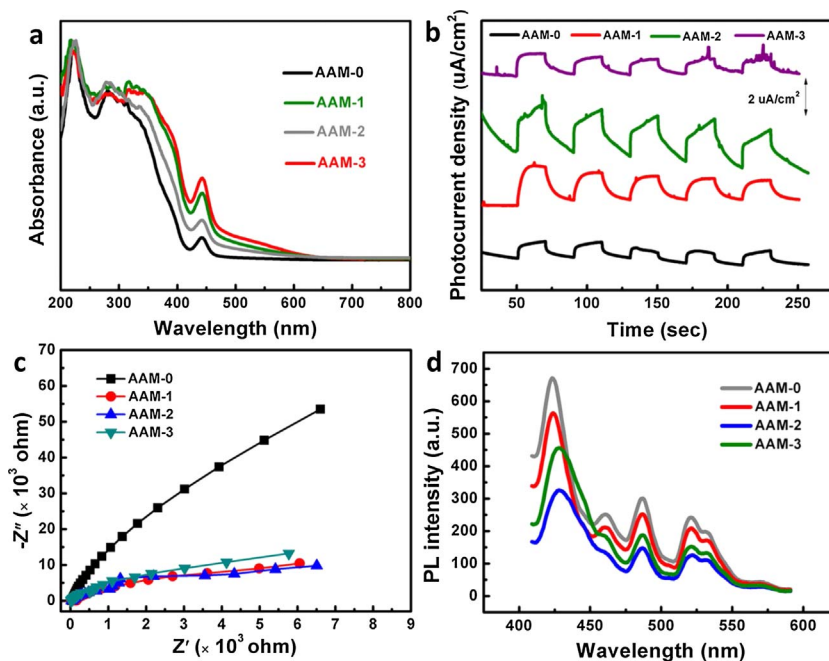


Fig. 7. (a) Photoreduction of Cr(VI) over different catalysts under visible light irradiation. (b) Photoreduction kinetics of Cr(VI) over different catalysts under visible light irradiation. (c) Comparison of the reaction rate constants of Cr(VI) photoreduction over different catalysts under visible light irradiation. (d) Recycling test on Cr(VI) photoreduction over Ag/AgCl/MIL-53-Fe (AAM-2) photocatalyst.



Cr(VI) under visible light irradiation.

To understand the behavior of photoexcited Ag/AgCl in Ag/AgCl@MIL-53-Fe photocatalytic systems, we first investigated the optical properties of the Ag/AgCl@MIL-53-Fe by means of UV-vis diffuse reflectance spectroscopy (DRS). Fig. 8a shows the DRS of Ag/AgCl@MIL-53-Fe samples. The bare MIL-53-Fe presents a typical DRS similar to previous reports, with an absorption edge onset around 479 nm, corresponding to the optical bandgap of 2.59 eV. The band at 220 nm is assigned to the ligand to metal charge transfer, implying the bonding of carboxylate oxygen to metal; while the bands in the range 300–600 nm are ascribed to the spin-allowed d-d transition of Fe^{3+} in MIL-53-Fe [13,28,29]. It is interestingly found that after the integration of Ag/AgCl, the AAM samples exhibit more intense absorption both in UV and visible regions. More specifically, the absorption intensity in the region of 300–600 nm is significantly enhanced, which could be contributed from the excitation of AgCl at wavelength below 400 nm and the SPR absorption of Ag at wavelength above 400 nm [30]. Such enhanced optical absorption would endow Ag/AgCl@MIL-53-Fe with more chance to interact and utilize incident light to produce much more active species for driving photocatalytic reaction. Obviously, the sources of photogenerated carriers and photocatalytic activity sites of MIL-53-Fe is greatly enriched after combination of plasmonic Ag/AgCl.

In addition to effect of optical absorption enhancement, the Ag/AgCl could also promote the photoinduced charge carrier separation. To probe the separation efficiency of photoinduced charge carriers, we studied the transient photocurrent response behaviors in photocatalytic Ag/AgCl@MIL-53-Fe systems. Fig. 8b shows current-time curves of MIL-53-Fe and Ag/AgCl@MIL-53-Fe with several on/off cycles under visible light irradiation. Clearly, all the catalysts are prompt in generating photocurrent with a reproducible response to on/off cycles. As generally accepted, a larger photocurrent density means a more efficient charge transfer and a slower recombination of photoinduced charge carriers. By combination with Ag/AgCl, the resulting Ag/AgCl@MIL-53-Fe samples exhibit the larger photocurrent density compared with the bare MIL-53-Fe. The photocurrent density of AAM-2 sample is about $2.0 \mu\text{A cm}^{-2}$, which is 3 times higher than that of bare MIL-53-Fe ($0.67 \mu\text{A cm}^{-2}$), indicating the more efficient separation and prolonged lifetime of photoinduced charge carriers in Ag/AgCl@MIL-53-Fe. Electrochemical impedance spectroscopy (EIS) Nyquist plots (Fig. 8c) were further examined to investigate the charge transfer and separation

Fig. 8. (a) UV-vis absorption spectra of MIL-53-Fe and Ag/AgCl@MIL-53-Fe. (b) Transient photocurrent responses of MIL-53-Fe and Ag/AgCl@MIL-53-Fe in 0.5 M Na_2SO_4 aqueous solutions under visible light irradiation. (c) EIS Nyquist plots of MIL-53-Fe and Ag/AgCl@MIL-53-Fe in 0.5 M Na_2SO_4 solution under dark condition. (d) PL spectra of MIL-53-Fe and Ag/AgCl@MIL-53-Fe with an excitation wavelength of 350 nm.

process in Ag/AgCl@MIL-53-Fe. Generally, the rapid charge transfer and efficient separation of photoinduced charge carriers are reflected by a smaller radius in EIS Nyquist diagram. Ag/AgCl@MIL-53-Fe samples show the smaller arc radius than that of bare MIL-53-Fe, indicating that the improved charge transfer process in Ag/AgCl@MIL-53-Fe. Fig. 8d shows the photoluminescence (PL) spectra of the bare MIL-53-Fe and Ag/AgCl@MIL-53-Fe (AAM-2). Clearly, PL intensity of the AAM-2 obviously diminished PL intensity, further indicating that the decoration of Ag/AgCl facilitates the charge transfer in MIL-53-Fe to effectively inhibit the recombination of photogenerated electrons and holes.

Based on the above results and discussion, the photocatalytic mechanism for the Ag/AgCl@MIL-53-Fe system is proposed and illustrated in Fig. 9. According to estimation from Mott-Schottky plots (Fig. S5, Supporting Information), the conduction band (CB) and valence band (VB) energy levels of MIL-53-Fe are about -0.50 and 2.09 V (vs. NHE), respectively. It can be excited under visible light due to the suitable bandgap energy of 2.64 eV. Notably, the MIL-53-Fe is difficult to oxidize OH^- to $\cdot\text{OH}$ radicals and can direct hole oxidation of RhB under visible light irradiation, because its VB value is lower than redox potential of $\cdot\text{OH}/\text{OH}^-$ (2.38 V vs. NHE) but is higher than the redox potential of RhB (1.43 V vs. NHE). As for Ag/AgCl, the AgCl cannot be excited by visible light due to its large band gap of 3.26 eV, while the

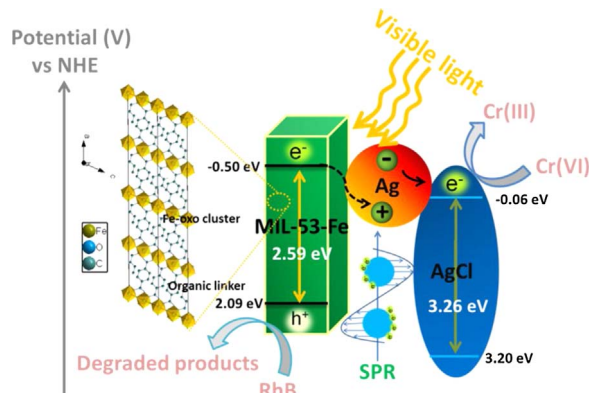


Fig. 9. Plasmonic Z-scheme photocatalytic mechanism of Ag/AgCl@MIL-53-Fe under visible light irradiation.

Ag can be SPR-excited under visible light irradiation. The SPR-excited electron would be transport from Ag to AgCl through Ag-AgCl interface due to the formed Schottky barrier resulting from the larger work function of Ag. Thus, the plasmonic Z-scheme photocatalytic process occurred in Ag/AgCl@MIL-53-Fe. Under visible light irradiation, the Ag is SPR-excited and the SPR-electron is injected into CB of AgCl to reduce Cr(VI) to Cr(III). The left positive charge species in Ag region are simultaneously recombine with the photogenerated electron from excited MIL-53-Fe to effectively promote the charge carrier separation in MIL-53-Fe, while the photoholes remain on MIL-53-Fe to oxidize RhB. The synergistic transfer of photoinduced electrons and holes in the Ag/AgCl@MIL-53-Fe ensure the long lifetime of charge carriers and yield the enhanced photocatalytic activity. More importantly, MIL-53-Fe as a typical metal-organic framework possesses the large surface area, intrinsic porosity and periodic arrangement. Such structure feature endows Ag/AgCl@MIL-53-Fe with open channels for efficient reactant diffusion and accommodation, which is favorable for the photocatalysis as well.

4. Conclusions

In summary, we have developed a facile one-pot solvothermal route to construct Ag/AgCl@MIL-53-Fe photocatalysts and demonstrated the efficient integration of plasmonic Ag/AgCl with MIL-53-Fe boost greatly the visible light photoreactivity of MOFs. The formed structure is in favor of the synergistic transfer of photoinduced electrons and holes in the Ag/AgCl@MIL-53-Fe via Z-scheme mechanism, ensuring the long lifetime of charge carriers and yield the enhanced photocatalytic activity. The photocatalytic experiments revealed that Ag/AgCl@MIL-53-Fe is highly efficient for dye degradation and Cr(VI) reduction under visible light irradiation, which is superior to that of bare MIL-53-Fe. Our finding on photoredox of Ag/AgCl@MIL-53-Fe would bring new insight into the design and development of highly efficient MOF-based photocatalysts.

Acknowledgements

This work was supported by the National Natural Science Foundation of China (51572227, 21771147), Sichuan Youth Science and Technology Foundation (2013JQ0012), Major Cultivating Foundation of Education Department of Sichuan Province (Grant 17CZ0036), Meritocracy Research Funds of CWNU (17YC007, 17YC017) and Innovative Research Team of CWNU (CXTD2017-1).

Appendix A. Supplementary data

Supplementary data associated with this article can be found, in the online version, at <http://dx.doi.org/10.1016/j.apcatb.2017.10.029>.

References

- [1] O.M. Yaghi, M.O.' Keeffe, N.W. Ockwig, H.K. Chae, M. Eddaoudi, J. Kim, *Nature* 423 (2003) 705–714.
- [2] N.L. Rosi, J. Eckert, M. Eddaoudi, D.T. Vodak, J. Kim, M. O'Keeffe, O.M. Yaghi, *Science* 300 (2003) 1127–1129.
- [3] J. Li, J. Sculley, H. Zhou, *Chem. Rev.* 112 (2012) 869–932.
- [4] J.Y. Lee, O.K. Farha, J. Roberts, K.A. Scheidt, S.T. Nguyen, J.T. Hupp, *Chem. Soc. Rev.* 38 (2009) 1450–1459.
- [5] M.A. Nasalevich, M. van der Veen, F. Kapteijn, J. Gascon, *CrystEngComm* 16 (2014) 4919–4926.
- [6] K.G.M. Laurier, F. Vermoortele, R. Ameloot, D.E. De Vos, J. Hofkens, M.B.J. Roeffaers, *J. Am. Chem. Soc.* 135 (2013) 14488–14491.
- [7] S. Wang, X. Wang, *Small* 11 (2015) 3097–3112.
- [8] Y. Li, H. Xu, S. Ouyang, J. Ye, *Phys. Chem. Chem. Phys.* 18 (2016) 7563–7572.
- [9] C.-C. Wang, J.-R. Li, X.-L. Lv, Y.-Q. Zhang, G. Guo, *Energy Environ. Sci.* 7 (2014) 2831–2867.
- [10] E.M. Dias, C. Petit, J. Mater. Chem. A 3 (2015) 22484–22506.
- [11] L. Ai, C. Zhang, L. Li, J. Jiang, *Appl. Catal. B* 148–149 (2014) 191–200.
- [12] C. Zhang, L. Ai, J. Jiang, *Ind. Eng. Chem. Res.* 54 (2015) 153–163.
- [13] C. Zhang, L. Ai, J. Jiang, *J. Mater. Chem. A* 3 (2015) 3074–3081.
- [14] M.J. Kale, T. Avanesian, P. Christopher, *ACS Catal.* 4 (2014) 116–120.
- [15] S.K. Dutta, S.K. Mehetor, N. Pradhan, *J. Phys. Chem. Lett.* 6 (2015) 936–944.
- [16] P. Wang, B.B. Huang, X.Y. Qin, X.Y. Zhang, Y. Dai, J.Y. Wei, M.H. Whangbo, *Angew. Chem. Int. Ed.* 47 (2008) 7931–7933.
- [17] P. Wang, B.B. Huang, X.Y. Zhang, X.Y. Qin, H. Jin, Y. Dai, Z.Y. Wang, J.Y. Wei, J. Zhan, S.Y. Wang, J.P. Wang, M.H. Whangbo, *Chem. Eur. J.* 15 (2009) 1821–1824.
- [18] C. Chen, W. Ma, J. Zhao, *Chem. Soc. Rev.* 39 (2010) 4206–4219.
- [19] S. Cao, J. Low, J. Yu, M. Jaroniec, *Adv. Mater.* 27 (2015) 2150–2176.
- [20] J. Yu, G. Dai, B. Huang, *J. Phys. Chem. C* 113 (2009) 16394–16401.
- [21] L. Ye, J. Liu, C. Gong, L. Tian, T. Peng, L. Zan, *ACS Catal.* 2 (2012) 1677–1683.
- [22] R. Qiao, M. Mao, E. Hu, Y. Zhong, J. Ning, Y. Hu, *Inorg. Chem.* 54 (2015) 9033–9039.
- [23] Y. Liang, S. Lin, L. Liu, J. Hu, W. Cui, *Appl. Catal. B* 164 (2015) 192–203.
- [24] S. Zhang, J. Li, X. Wang, Y. Huang, M. Zeng, J. Xu, *ACS Appl. Mater. Interfaces* 6 (2014) 22116–22125.
- [25] L. Ai, L. Li, C. Zhang, J. Fu, J. Jiang, *Chem. Eur. J.* 19 (2013) 15105–15108.
- [26] M. Nocchetti, A. Donnadio, V. Ambrogi, P. Andreani, M. Bastianini, D. Pietrella, L. Latterini, *J. Mater. Chem. B* 1 (2013) 2383–2393.
- [27] J. Liu, R. Li, Y. Hu, T. Li, Z. Jia, Y. Wang, Y. Wang, X. Zhang, C. Fan, *Appl. Catal. B* 202 (2017) 64–71.
- [28] G.-T. Vuong, M.-H. Pham, T.-O. Do, *Dalton Trans.* 42 (2013) 550–557.
- [29] G.-T. Vuong, M.-H. Pham, T.-O. Do, *CrystEngComm* 15 (2013) 9694–9703.
- [30] R. Dong, B. Tian, C. Zeng, T. Li, T. Wang, J. Zhang, *J. Phys. Chem. C* 117 (2013) 213–220.